

This is the accepted manuscript made available via CHORUS. The article has been published as:

Influence of Elastic and Surface Strains on the Optical Properties of Semiconducting Core-Shell Nanoparticles

John Mangeri, Olle Heinonen, Dmitry Karpeyev, and Serge Nakhmanson

Phys. Rev. Applied **4**, 014001 — Published 7 July 2015

DOI: [10.1103/PhysRevApplied.4.014001](https://doi.org/10.1103/PhysRevApplied.4.014001)

Elastic and surface strain influence on optical properties of semiconducting core-shell nanoparticles

John Mangeri*

Department of Physics, University of Connecticut, Storrs, Connecticut 06269, USA

Olle Heinonen

*Material Science Division, Argonne National Laboratory, Lemont, Illinois 60439, USA and
Center for Hierarchical Material Design, Northwestern-Argonne Institute of Science and Engineering,
Northwestern University, Evanston, Illinois 60208, USA*

Dmitry Karpeyev

Computation Institute, University of Chicago, Chicago, Illinois 60637, USA

Serge Nakhmanson

*Department of Materials Science & Engineering and Institute of Material Science,
University of Connecticut, Storrs, Connecticut 06269, USA and
Department of Physics, University of Connecticut, Storrs, Connecticut 06269, USA*

(Dated: June 15, 2015)

Core-shell nanoparticle systems of Zn-ZnO and ZnO-TiO₂ are studied computationally using finite element methods. The inclusion of a surface free energy and the elastic mismatch of the core and shell create an imprinting effect within the shell structure that produces a wide variation of strains. Due to this diversity of strains, the sharp direct band gap edges of the bulk semiconductor are observed to be broadened. We show that a variety of factors, such as particle size, core-to-shell volume ratio, applied hydrostatic pressure, shell microstructure, as well as the effect of elastic anisotropy, can influence the distribution of optical band gap values throughout the particle.

I. INTRODUCTION

Composite core-shell nanoparticles (CSNPs) exhibit functional behavior, involving combinations of electronic, magnetic, and chemical properties, that is not being observed in their bulk-level constituent materials. A wide range of possible functionalities, coupled with the ease of fine-tuning them by controlling particle size, shape and microstructure, make these nanocomposites highly attractive for a broad range of possible applications, spanning from catalysis[1–3], biomedical imaging[4–7] and drug delivery[8, 9], environmental remediation[10–12] to electro-magnetic radiation sensing, absorption and shielding.[13–16] Core-shell nanoparticles with semiconducting shells, in particular those composed of metal oxides, such as ZnO[17] and TiO₂[18], are currently being investigated for the enhancement of their optical properties[16, 19–24] and photocatalytic activity, as well as for the efficiency improvement in photovoltaic devices.[16, 25, 26]

Modern state-of-the-art synthetic techniques permit fabrication not only of spherical core-shell geometries, but also of a variety of different nanostructures, including cubes, hexagons, disks, rods, tubes and etc.[16] For example, in addition to spherical shapes,[17, 27, 28] ZnO-based structures have been manufactured in the form of nanowires,[29] hollow hexagonal nanotubes[30–32] and nanodisks (with Zn core).[33] It was also demonstrated that distinct ZnO shell morphologies, such as single-crystal, polycrystalline or mesoporous ones, can be produced,[33] or that ZnO nanorods can be grown ra-

dially around a spherical Zn core.[34, 35] Furthermore, the core-to-shell size ratio of spherical Zn/ZnO CSNPs can be controlled during synthesis,[17, 27, 28] allowing for even better fine-tuning of their microstructure and, consequently, the associated functional properties that may depend on it.

On the other hand, ZnO nanoparticles and wire-, and rod-like structures can also be utilized as cores around which shells made up of another material can be grown. TiO₂, in a variety of different phases, is a popular choice for the latter. [1, 2, 18, 21, 25, 26, 36–39] Some of the resulting nanocomposites were recently evaluated as promising solar-cell components, revealing that their performance strongly depends on the thickness of the TiO₂ coating.[25, 26]

In the course of these investigations, it was realized that such nanostructures display significant deviations from the optical properties of their bulk constituent components — including the measured values of their band gaps E_g . [17, 27, 28, 31, 34, 40, 41] Although quantum confinement effects that become important on the length scale of few nm are expected to affect the E_g , deviations from bulk behavior were found even in CSNPs that are too large to operate in the quantum confinement regime.

It is, however, reasonable to assume that a range of other factors that are related to the intricate CSNP geometry and microstructure may be behind the observed optical properties variation or, alternatively, could be used for further property modification. Even for a simple case of a perfectly spherical CSNP, such factors may include both type and curvature of the shell surface, core-

to-shell volume ratio, shape of the core, misfit strains at the core/shell interface or between differently oriented grains within a polycrystalline shell, as well as elastic behavior of the particle under applied mechanical loads, such as, e.g., hydrostatic pressure.

In this work, utilizing a finite-element method (FEM) based computational approach with materials parameters fitted from *ab initio* simulations, we have studied the influence of the aforementioned elastic, morphological and microstructural factors on the internal stress fields developed within spherical CSNPs. This information was then used to evaluate the stress-induced distribution of band-gap values throughout the particle volume. Two combinations of core/shell constituent materials were considered: [i] Zn core and wurtzite (*w*-) ZnO shell and [ii] *w*-ZnO core and rutile (*r*-) TiO₂ shell, representing, as discussed in detail below, two very different elastic cases. Our work demonstrates that non-uniform internal stresses that exist in composite core-shell particles due to their complex morphology and microstructure result in formation of band tails (rather than sharp band edges) — resembling a similar phenomenon in amorphous Si[42] — however, the magnitude of this effect in ZnO and TiO₂ shells is limited due to a rather weak variation of E_g with applied stress in these materials. Nevertheless, the methodology presented here can be applied for predictive identification of core/shell materials combinations possessing a stronger response with respect to internal stress fields, as well as fine-tuning their properties by manipulating the geometrical parameters and microstructure of the nanoparticle.

II. COMPUTATIONAL DETAILS

A. Structural models

CSNP models utilized in this investigation were created and meshed using CUBIT[43]. Model variants with spherical and faceted monocrystalline cores are presented in panels (a) and (b) of Fig. 1, respectively. Each of these core types was combined with either a monocrystalline (uniform) shell or a polycrystalline shell with a radial arrangement of grains, as shown in the panels. The latter shell structures were made by carrying out a Voronoi tessellation on the surface of a sphere using the VORO++[44, 45] software package and include from 10 to 20 separate material blocks, which represent crystalline grains. Specific number of grain regions within this range was found not to affect the obtained results strongly.

Various crystallographic orientations of the elastic stiffness tensor axes within each shell block, or within a uniform shell, with respect to their orientations in the core region were considered. Possible mutual arrangements of the core/shell elastic stiffness tensor axes are shown in Fig. 1(c) and include (going from left to right) uniform collinear, uniform non-collinear, polycrystalline radial and polycrystalline random. Positioning of the ten-

sor axes within each shell block was performed by an $\mathbf{Z}_1(\theta)\mathbf{X}_2(\phi)\mathbf{Z}_3(\Psi)$ sequence of Euler rotations. For example, the [111] orientation of the shell elastic stiffness tensor axes with respect to those within the core was made by setting $\theta = 0^\circ$, $\phi = 54.74^\circ$, and $\Psi = 45^\circ$.

For the chosen combination of the core type and shell microstructure, the total CSNP diameter D was varied from 8 to 50 nm, keeping its size in the weak to no quantum confinement regime.[31, 46–48] In addition, the core/shell volume ratio was also changed, ranging from 0.15 to 0.86, for a total of 120 different models processed.

Finally, we should point out that the computational approach, described in details below, cannot yet be utilized directly to predict optimal core or particle shapes, or the location of the core inside the particle — e.g., the stress induced off-centering and asymmetric shapes of cores in some metal alloy particles.[49–52] Nevertheless, for prescribed core and shell shapes, and their locations, this method can serve as means for rapid (compared to atomistic simulations) evaluation of the resulting stress fields and the associated elastic energies. Although only spherical and faceted cores, and spherical particles with centered core locations are considered here, more elaborate CNSP models can be created in CUBIT, including those with non-centered cores and faceted shells that may have different surface properties specified for different facets.

B. Bulk elastic energy

CNSP models presented in the previous subsection were used as spatial domains of volume Ω enclosed by a surface S . The elastic energy (within the linear elasticity approximation) of a bulk system of volume Ω is given by

$$\begin{aligned} E_{\text{bulk}} &= \int_{\Omega} \sigma_{ij} \epsilon_{ij} dV = \frac{1}{2} \int_{\Omega} C_{ijkl} \epsilon_{kl} \epsilon_{ij} dV \\ &= \frac{1}{8} \int_{\Omega} C_{ijkl} \left[\frac{\partial u_k}{\partial x_l} + \frac{\partial u_l}{\partial x_k} \right] \left[\frac{\partial u_i}{\partial x_j} + \frac{\partial u_j}{\partial x_i} \right] dV. \end{aligned} \quad (1)$$

Here σ_{ij} , ϵ_{kl} and C_{ijkl} are elastic stress, strain and stiffness tensors, respectively, and $u_k(\mathbf{r})$ are vector components of the displacement field with Cartesian components indicated by the indices $i, j, k, l = x, y, z$; summation over repeated Cartesian indices is implied.

The material specific values of the individual components of the C_{ijkl} tensor, as well as the orientation of its main axes, could be chosen independently for each structural block within the model. For the materials involved, i.e., metallic Zn, *w*-ZnO and *r*-TiO₂, bulk C_{ijkl} values were taken from the literature and are assembled in Table I. It is noteworthy, that although formally *w*-ZnO has hexagonal symmetry (space group $P6_3mc$), it is nearly isotropic elastically since — utilizing Voigt notation for the indices in what follows — its $C_{11} \simeq C_{33}$, $C_{12} \simeq C_{13}$ and $C_{44} \simeq C_{66} \simeq (C_{11} - C_{12})/2$. For Zn $C_{33} \simeq C_{11}/3$, while for ZnO $C_{33} \simeq C_{11}/2$, which makes both of these

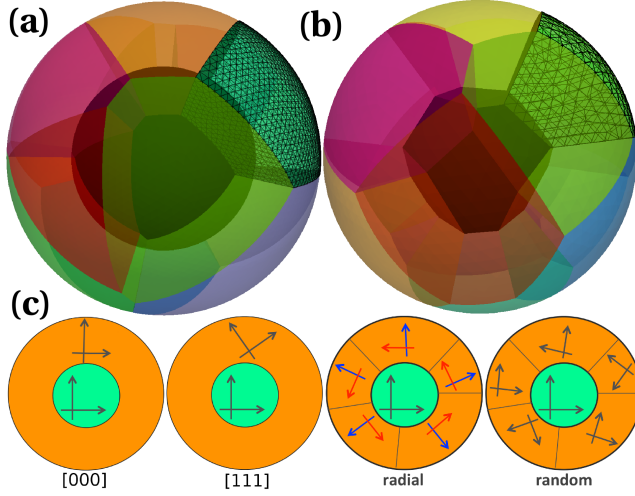


FIG. 1. Sketches of polycrystalline-core CSNP models with (a) spherical and (b) faceted monocrystalline cores. Tetrahedral FEM meshes are also shown in some shell blocks. (c) Going from left to right: uniform collinear [000], uniform non-collinear (example for the [111] shell axes orientation), polycrystalline radial and polycrystalline random mutual arrangements of the core/shell elastic stiffness tensor axes. In the radial arrangement, a hexagonal (*w*-ZnO) or tetragonal (*r*-TiO₂) symmetry axis in each shell block is pointing outward along the external surface normal, while the orientation of the other two axes is chosen randomly. See text for more details.

TABLE I. Bulk elastic stiffness tensor components for metallic Zn, *w*-ZnO and *r*-TiO₂ in reduced Voigt notation[53] in units of GPa. Averaged components for an isotropic case[53] with $C_{11} = C_{33} = 2\mu + \lambda$, $C_{12} = C_{13} = \lambda$ and $C_{44} = C_{66} = \mu$ are also given for both shell materials.

	Ref.	Crystal structure	C_{11}	C_{12}	C_{13}	C_{33}	C_{44}	C_{66}
Zn	[54]	hcp ($P6_3/mmc$)	163.0	30.6	48.1	60.3	39.4	65.9
ZnO	[55]	wurtzite ($P6_3mc$)	209.7	121.1	105.1	210.9	42.5	44.3
		isotropic	205.9	118.5			43.7	
TiO ₂	[56]	rutile ($P4_2/mnm$)	268.0	174.9	147.4	484.2	123.8	190.2
		isotropic	362.3	136.1			113.1	

structures highly anisotropic. Therefore, Zn/*w*-ZnO and *w*-ZnO/*r*-TiO₂ core/shell combinations represent two drastically different elastic cases — i.e., anisotropic core/isotropic shell and isotropic core/anisotropic shell — that warrant an interesting comparison of the resulting properties.

C. Surface elastic energy

Since surface-to-volume ratio in CSNPs is rather large, size effects related to surface elasticity could result in significant contributions to the total free energy of such particles. To account for these effects, the Gurtin-Murdoch approach[57] is adopted here. The energy contribution from surface elasticity is given by

$$E_{\text{surface}} = \int_S \sigma_{\alpha\beta}^s \epsilon_{\alpha\beta}^s dS, \quad (2)$$

where the indices $\alpha, \beta, \delta, \gamma = 1, 2$ are denoting the components a local (two-dimensional) orthonormal basis ($\mathbf{e}_1, \mathbf{e}_2$) in the tangent plane of the surface S . In this expression, we use superscript $(\dots)^s$ to denote surface-specific quantities. The surface stress $\sigma_{\alpha\beta}^s$ in Eq. (2) is related to the surface elastic stiffness tensor $C_{\alpha\beta\gamma\delta}^s$ through

$$\sigma_{\alpha\beta}^s = \tau_{\alpha\beta} + C_{\alpha\beta\delta\gamma}^s \epsilon_{\delta\gamma}^s, \quad (3)$$

where $\tau_{\alpha\beta}$ are the residual surface stress tensor components.

Unlike the bulk elastic stiffness coefficients C_{ijkl} , surface elastic parameters $\{C_{\alpha\beta\delta\gamma}^s, \tau_{\alpha\beta}\}$ are not usually available from experiments. However, they can (in principle) be obtained from atomistic first-principles calculations carried out for thin material slabs. For both *w*-ZnO and *r*-TiO₂, elastic parameters for a variety of different crystallographic surfaces have been evaluated with the help of these techniques, as reported in Refs. [58] and [59], respectively. In this investigation, it is assumed that regardless of the bulk elastic tensor orientation with the (poly- or monocrystalline) particle shell, only the lowest energy surfaces are formed on its exterior, i.e., (10 $\bar{1}$ 0) for *w*-ZnO and (110) for *r*-TiO₂. Furthermore, although due to the anisotropy of these surfaces $\tau_1 \neq \tau_2$, both components are much smaller than the associated $C_{\alpha\beta\gamma\delta}^s$ parameters and thus an approximation of $\tau_{\alpha\beta} = \tau \delta_{\alpha\beta}$ is

TABLE II. Elastic stiffness tensor components in reduced Voigt notation[53] and averaged residual stresses τ for the (10 $\bar{1}$ 0) *w*-ZnO and (110) *r*-TiO₂ surfaces in units of N/m.

	Ref.	C_{11}^s	C_{12}^s	C_{66}^s	C_{22}^s	τ
<i>w</i> -ZnO (10 $\bar{1}$ 0)	[58]	49.1	15.1	13.7	34.9	-1.7
<i>r</i> -TiO ₂ (110)	[59]	-73.8	-26.3	0.0	-17.7	1.8

used, where τ is an average of the two components. The values of the surface elastic parameters $\{C_{\alpha\beta\delta\gamma}^s, \tau\}$ used in this study are presented in Table II.

D. Solving for the displacement field

For each CSNP model, the equilibrium displacement field was computed by minimizing elastic energy $E_{\text{bulk}} + E_{\text{surface}}$ defined by Eqs. (1) and (2) over domain Ω . The equivalent partial differential equation formulation, defined by the vanishing of the energy variation, was cast in the Galerkin weak form and solved for the displacement field $\{u_i(\mathbf{r})\}$. Displacements were drawn from the space of piecewise linear continuous functions P_1 on the tetrahedral mesh discretizing Ω and satisfying the appropriate boundary conditions. Two different types of boundary conditions were used: a vanishing pressure (normal stress) and a prescribed nonzero pressure; note that the tangential strains were constrained by the surface stresses. To carry out this numerical procedure we used an FEM code FERRET[62] that is being developed by the authors based on the MOOSE simulation framework.[63–66] The surface stress and strain tensors were constructed out of their bulk counterparts with the help of the projection operator[58] $\mathbf{P} = \mathbf{1} - \mathbf{n}(\mathbf{r}) \otimes \mathbf{n}(\mathbf{r})$, where $\mathbf{n}(\mathbf{r})$ is the outward pointing normal unit vector to S at a given quadrature point:

$$\sigma^s = \mathbf{P}\sigma\mathbf{P} \text{ and } \epsilon^s = \mathbf{P}\epsilon\mathbf{P}. \quad (4)$$

In each calculation the relative residual norm was converged to less than 10^{-8} , irrespective of the applied boundary conditions or any specific variations within the domain Ω , such as utilizing spherical or faceted cores, or changing the core/shell volume ratio.

E. Coupling the band gap to stress fields

Variations of the values of the electronic band gap E_g under applied stress fields have also been evaluated with the help of first-principles computational techniques for w -ZnO[60] and r -TiO₂.[61] These calculations provided linearized expressions — within the deformation potential theory[67, 68] — for the E_g dependence on biaxial

$\sigma_b = \sigma_1 \equiv \sigma_2$ and uniaxial $\sigma_u = \sigma_3$ stresses in both materials:

$$E_g = E_g^0 + \delta E = E_g^0 + c_b\sigma_b + c_u\sigma_u, \quad (5)$$

where coefficients c_b and c_u are the biaxial and uniaxial band-gap stress rates, respectively. Their values, as well as those of unstrained band gap energies used in this investigation are assembled in Table III.

III. RESULTS AND DISCUSSION

A. Stress fields

The simultaneous solution of the volume and surface elastic problems for a given CSNP model produces a position-dependent displacement field $\{u_i(\mathbf{r})\}$, from which all the components of the (non-uniform) stress and strain tensors can be obtained in a standard way. Typical results of such simulations for the σ_3 stress tensor component are presented as three-dimensional maps in Fig. 2(a-b) for a particle with a spherical core 15 nm in diameter and a 5 nm thick monocrystalline shell around it (total diameter 25 nm), kept under condition of vanishing external pressure.

These maps are supplemented by histograms in panels (c-d), showing how the values of the principal stresses σ_1 , σ_2 and σ_3 are distributed throughout the volume of the shell. In the case of a Zn/ w -ZnO particle [panels (a) and (c)], it was found that its shell expands slightly in order to satisfy the vanishing external pressure condition, which results in tensile stresses at the core/shell interface. On the other hand, a w -ZnO/ r -TiO₂ particle [panels (b) and (d)] contracts under the same conditions, which leads to emerging compressive interfacial stresses. In both instances, we observed anisotropic distribution of stresses throughout the shell volume. Specifically, in the Zn/ w -ZnO particle oriented as shown in Fig. 2(a), the hcp Zn core is stiffer within the xy plane and softer along the z axis (see Table I), and this elastic anisotropy imprints itself onto the interfacial region of the nearly isotropic w -ZnO shell in the form of a varying stress field. Also, as expected from the materials symmetry, in both particles the obtained shell volume distributions of principal stresses σ_1 and σ_2 were similar to each other, with the one for σ_3 being noticeably different, which is in agreement with the approximation utilized in the fitting of Eq. 5. Finally, in both particles, stress fields on or close to the external surface (omitted in Fig. 2(a-b) for the sake of clarity) were found to be smaller, but nonetheless about the same order of magnitude as the shell-volume stresses discussed above.

B. Band gap distributions

Fig. 3 shows variations of the CSNP band gap δE (see Eq. 5) throughout the shell volume. These plots are

TABLE III. Parameterized biaxial and uniaxial band-gap stress rates, as well as unstrained band gap energies for w -ZnO and r -TiO₂.

		Stress rate [10^{-1} eV/GPa]	Method + Ref.	E_g^0 [eV]
w -ZnO	c_b	−0.02	HSE+ G_0W_0 [60]	3.20
	c_u	−0.32		
r -TiO ₂	c_b	−0.07	GGA [61]	3.02
	c_u	0.08		

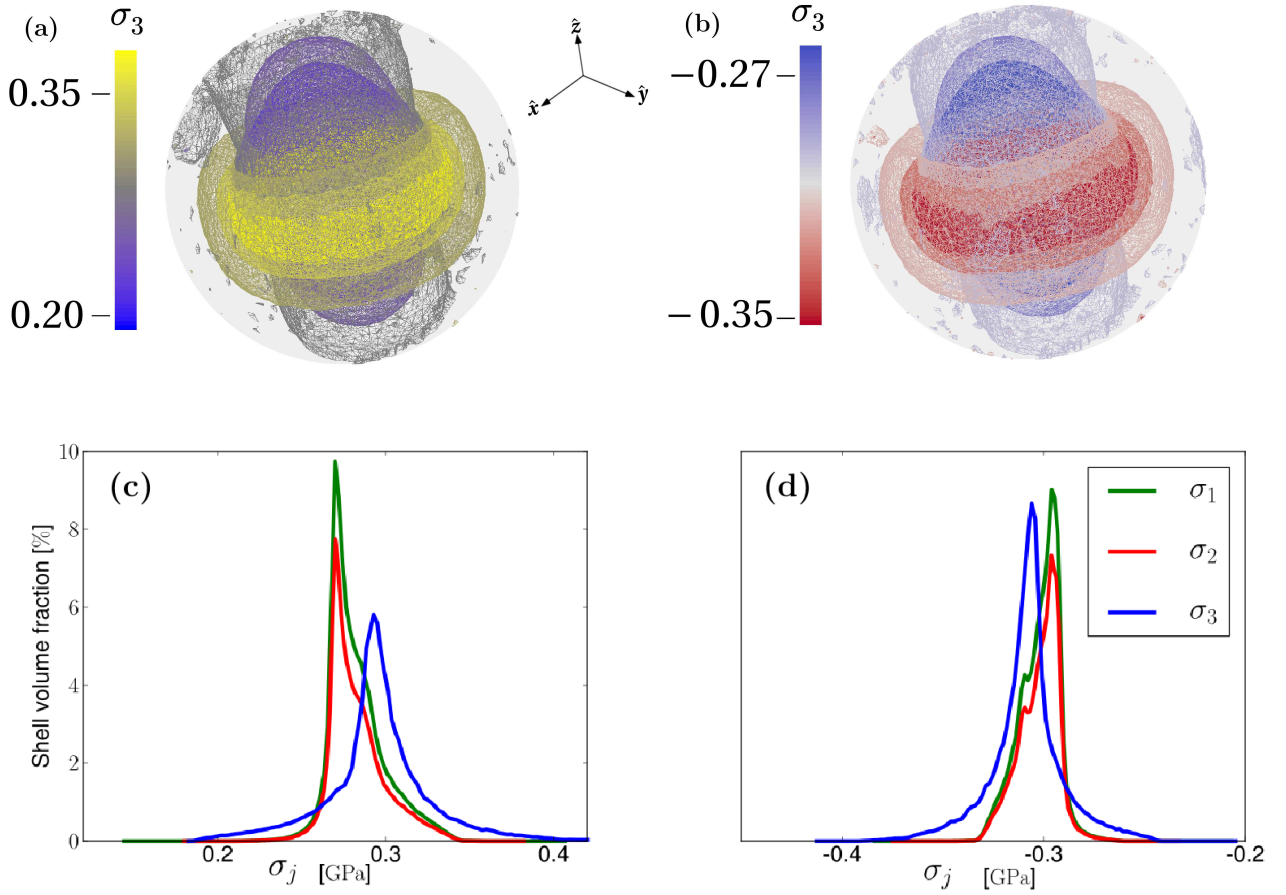


FIG. 2. Three-dimensional maps [panels (a) and (b)] and corresponding shell-volume distribution histograms [panels (c) and (d)] of the principal stress fields within a CSNP with a spherical core 15 nm in diameter and a 5 nm thick monocrystalline shell around it (total diameter 25 nm), kept under condition of vanishing external pressure. Panels (a) and (c): tensile stresses in a Zn/*w*-ZnO particle. Panels (b) and (d): compressive stresses in a *w*-ZnO/*r*-TiO₂ particle. In both cases, the particle core/shell elastic stiffness tensor axes are collinear and their orientations coincide with those of the global coordinate system, whose axes are shown in the insert. For the sake of clarity, stress fields on the particle surface, or areas close to it, are not shown in panels (a) and (b).

also presented as histograms, similar to those included in Fig. 2(c-d), for particles with different shell morphologies, but having the same total diameter of 25 nm, as well as the core region of approximately 15 nm in size. Same as before, all of the calculations here are done for the condition of vanishing external pressure. Panels (a) and (c) on the left describe the Zn/*w*-ZnO core/shell materials combination, while panels (b) and (d) on the right refer to the *w*-ZnO/*r*-TiO₂ combination. The top (bottom) panel rows are for the systems with spherical (faceted) cores, respectively. For each specific materials/core-geometry configuration, band gap distributions — obtained from the stress field calculations with the help of parametrization in Eq. 5 — are shown for a number of different shell structures, as outlined in Fig. 1(c).

From the data presented in Fig. 3 we can make the following observations: [i] For all of the considered materials/core-geometry combinations, most of the band-gap energies distributed throughout the shell vol-

ume are smaller than the bulk value E_g^0 . [ii] For both core/shell materials combinations, the distribution curves for spherical and faceted cores look different, with the ones for the spherical core showing a greater range of possible band-gap energies. [iii] For both core/shell materials combinations, shell morphology does not have a strong influence over shaping the form of the band-gap energy distribution curve. Random shell configuration for the *w*-ZnO/*r*-TiO₂ case may be a mild exception here. [iv] In all these cases, the intensity of the remaining elastic stresses within the CSNP that is relaxed to vanishing external pressure (no more than approx. 0.4 GPa; see Fig. 2) can produce only minor shifts in the size of the band gap: 50–60 meV in case of Zn/*w*-ZnO and much smaller for *w*-ZnO/*r*-TiO₂.

In Fig. 4 we show the dependence of the band-gap energy distributions throughout the shell volume on the change in particle diameter D at fixed core-to-shell volume ratio (top panels), or the change in core-to-shell vol-

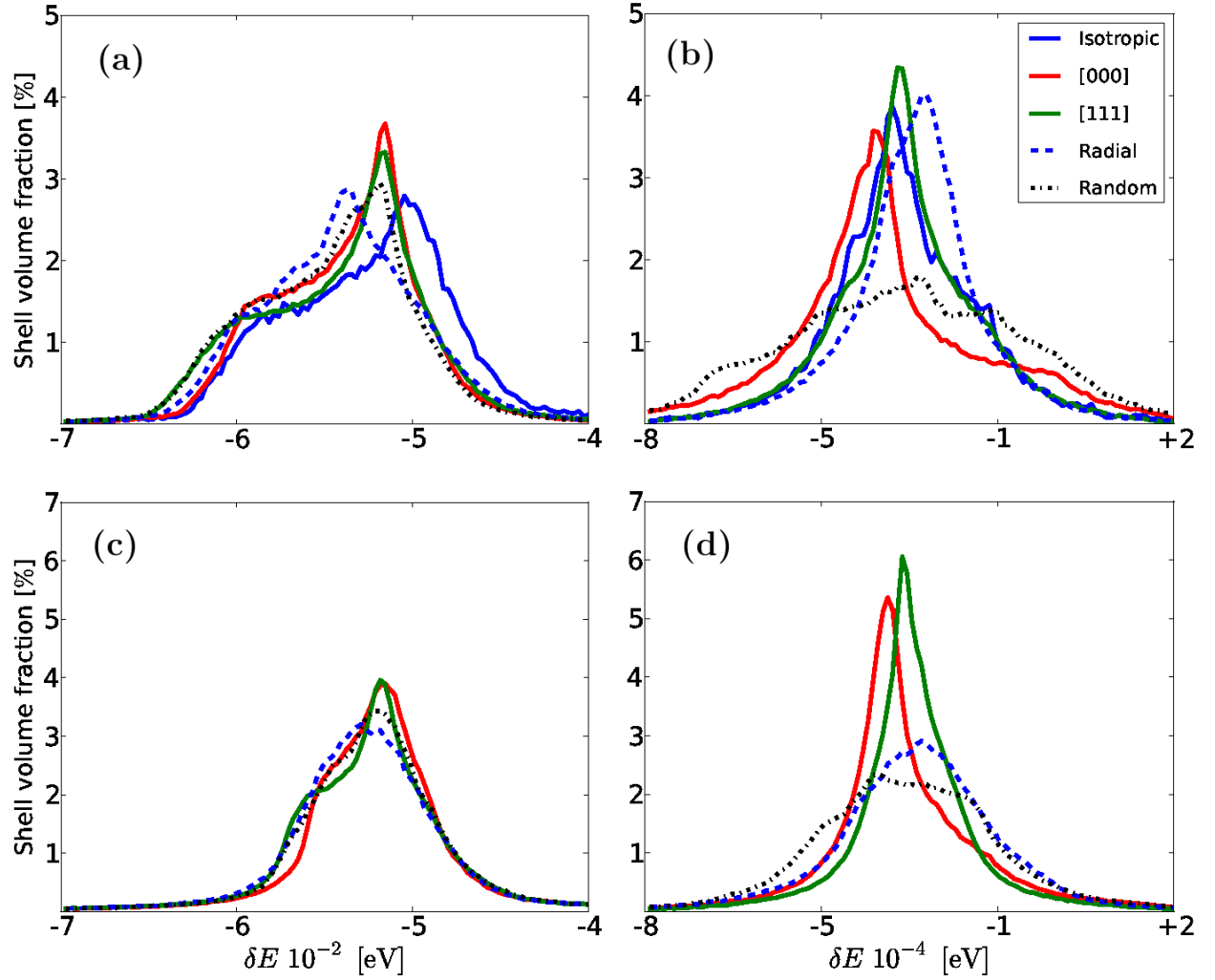


FIG. 3. Histogram plots showing distribution of CSNP band-gap energies δE (as parametrized in Eq. 5) throughout the shell region of the particle for a variety of different shell morphologies at vanishing external pressure. See panel (c) of Fig. 1 and the accompanying caption for the detailed descriptions of the latter. (a) Zn/*w*-ZnO core/shell materials combination with a spherical core. (b) *w*-ZnO/*r*-TiO₂ core/shell materials combination with a spherical core. (c) Zn/*w*-ZnO core/shell materials combination with a faceted core. (d) *w*-ZnO/*r*-TiO₂ core/shell materials combination with a faceted core. Here, isotropic shell morphology refers to a shell material where the elastic stiffness tensor components are averaged out to isotropic symmetry (see Table I for further details).

ume ratio, expressed through the changing core radius r , at fixed particle diameter (bottom panels). All the particles used in these calculations have spherical cores that are combined with monocrystalline collinear shells and were relaxed under condition of vanishing external pressure. As in the case of the previous figure, panels (a) and (c) on the left describe the Zn/*w*-ZnO core/shell materials combination, while panels (b) and (d) on the right refer to the *w*-ZnO/*r*-TiO₂ combination.

As can be seen from the top row of panels, the distribution of band-gap energies narrows as D is increased and its average value shifts closer to that of the bulk band-gap opening E_g^0 . On the other hand, reducing D below 25 nm produces wider band-gap energy distributions, compared to those shown in Fig. 3, as well as moves the average E_g

value further down, e.g., by up to -0.13 eV in a Zn/*w*-ZnO CSNP that is 10 nm in diameter. However, when the core radius is varied while keeping the particle diameter fixed, a different behavior is observed. For particles with large core radii (narrow shell regions) wide distributions of band gap variations δE are produced, while for particles with small radii (wide shell regions) rather sharply defined values of $E_g < E_g^0$ are obtained.

In Fig. 5 we present the dependence of the variation of the particle shell band-gap energy δE on the applied hydrostatic pressure p for both the Zn/*w*-ZnO (top) and *w*-ZnO/*r*-TiO₂ (bottom) core/shell materials combinations. These results were obtained for a CSNP model with a 15 nm spherical core and a 5 nm thick monocrystalline shell ($D = 25$ nm) that was set up in

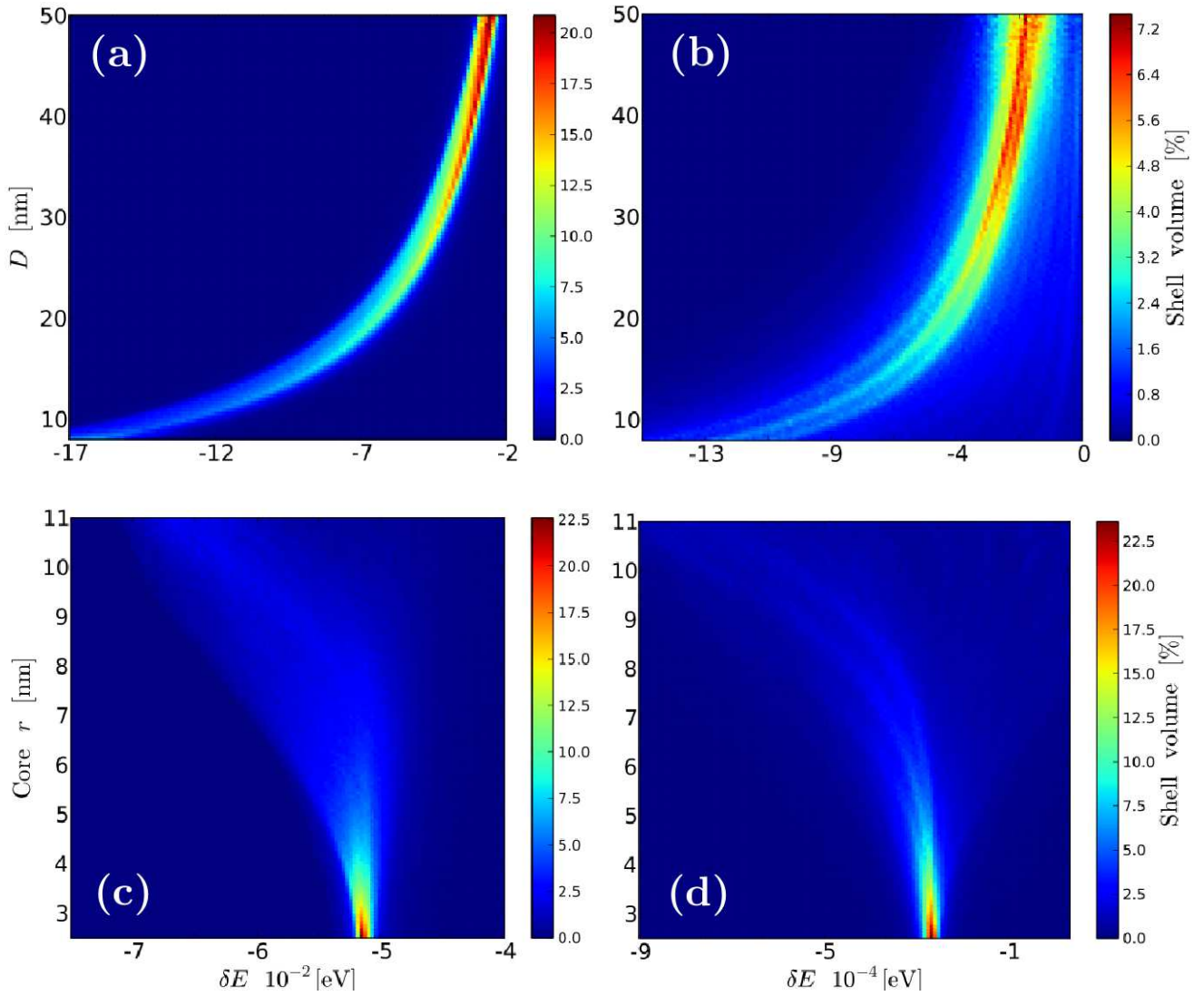


FIG. 4. Contour plots showing the dependence of the CSNP band-gap energy distributions throughout the shell volume on particle diameter D at fixed core-to-shell volume ratio (top panels), or core radius r at fixed particle diameter (bottom panels). In the former case, the core-to-shell volume ratio is fixed at 0.276, while in the latter case $D = 25$ nm. Left panels (a) and (c) refer to the Zn/ w -ZnO system; right panels (b) and (d) refer to the w -ZnO/ r -TiO₂ system. Combinations of spherical cores and monocrystalline collinear shells are used in all the calculations presented here, with the CSNP shapes relaxed under condition of vanishing external pressure.

either a collinear or an isotropic configuration. As can be seen from the data shown, the band gaps change differently under hydrostatic compression in Zn/ w -ZnO and w -ZnO/ r -TiO₂ CSNPs. In the former system, $\delta E(p) > 0$ and, therefore, the band gap increases — and does so quite substantially, e.g., growing by 1 eV for $p = 5$ GPa. On the other hand, in the latter system, due to canceling out of contributions from uniaxial and biaxial stresses ($c_b \simeq -c_u$, see Table III), $\delta E(p)$ is small and negative, i.e., the band gap decreases under pressure, but only by a few meV. We should point out that under pressures in between 8.3 and 9 GPa ZnO undergoes a phase transition from wurtzite to a rock-salt phase, however, this transformation is not considered here.

C. Band gap sensitivity to mutual arrangement of core/shell elastic stiffness tensor axes

As shown in Fig. 3, our investigation had identified some differences in the shell-volume band-gap energy distributions of monocrystalline collinear [000] and non-collinear (e.g., [111]) mutual arrangements of core/shell elastic stiffness tensor axes for both of the considered materials systems. In Fig. 6 we present the changes of the volume-weighted variance of the band-gap energy E_g with respect to all of the symmetrically inequivalent Euler rotations \mathbf{Z}_1 ($\theta = 0$) \mathbf{X}_2 (ϕ) \mathbf{Z}_3 (Ψ) of the orientations of the shell elastic stiffness tensor axes. Again, the orientation of the elastic stiffness tensor axes of the core

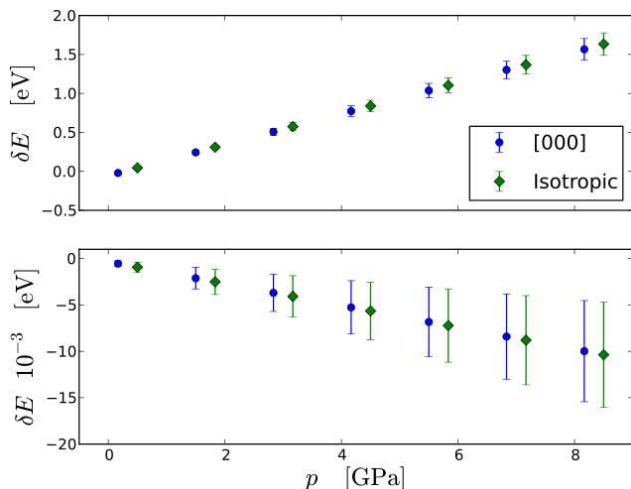


FIG. 5. Dependence of the variation of the particle shell band-gap energy δE on the applied hydrostatic pressure. Top: Zn/*w*-ZnO system. Bottom: *w*-ZnO/*r*-TiO₂ system. In all calculations presented here, a CSNP model with a 15 nm spherical core and a 5 nm thick monocrystalline shell ($D = 25$ nm) was used. Results for collinear and isotropic shells are depicted by full circles and diamonds, respectively. Error bars attached to the symbols represent volume-weighted standard δE deviations that show the broadening of the band-gap energy distributions under increasing compressive pressure.

region is chosen as $\theta, \phi, \Psi \equiv 0$ and the calculations are done for a particle with $D = 25$ nm and core/shell volume ratio of 0.276 at the condition of vanishing external pressure. Although the variance of the band-gap energy is small in both of the considered materials systems, the differences in the plot symmetry are quite pronounced between them, with dissimilar combinations of rotation angles ϕ and Ψ required to achieve the largest variance.

IV. CONCLUSIONS

In this investigation, we have utilized a finite element method to study the elastic properties of CSNPs with a variety of different shell morphologies, including mono- and polycrystalline configurations. Two different core types, faceted and spherical, as well as two popular core/shell materials combinations, Zn/*w*-ZnO and *w*-ZnO/*r*-TiO₂, were considered. The connections between the elastic stresses within the particles and their optical properties — as reflected in the shell-volume distributions of the band-gap energy values — were examined with the help of simple fits obtained for *w*-ZnO and *r*-TiO₂ bulk crystals by quantum mechanical calculations.[60, 61] Our investigation shows that the band gap shifts that could be achieved for these two shell materials in the spherical particle geometry are not large under vanishing external pressure and only weakly depend on the shell morphology. However, in the case of *w*-ZnO, reducing the particle size to below 20 nm and/or

applying hydrostatic pressure on the order of few GPa can cause substantial changes in the average value of its band gap. In *r*-TiO₂, the band gap energy changes due to applied pressure and elastic anisotropy remain uniformly small (on the order of a few meV) for all the considered particle geometries and simulation conditions. In this regard, the anatase TiO₂ polymorph (not studied here) may be a better choice of a shell material for potential photovoltaic applications, since, according to Ref. 61 its E_g should display a much larger variation under applied stress.

ACKNOWLEDGMENTS

Part of the work by O.H. was performed under the following financial assistance award 70NANB14H012 from U.S. Department of Commerce, National Institute of Standards and Technology as part of the Center for Hierarchical Material Design (CHiMaD). The authors gratefully acknowledge the computing resources provided on Blues, a high-performance computing cluster operated by the Laboratory Computing Resource Center at Argonne National Laboratory, and on the Hornet cluster hosted by the Taylor L. Booth Engineering Center for Advanced Technology (BECAT) located at the University of Connecticut at Storrs. Part of the work at Argonne was funded by the Department of Energy. The authors are also indebted to Prof. Luyi Sun for many useful discussions and help with providing references for this paper.

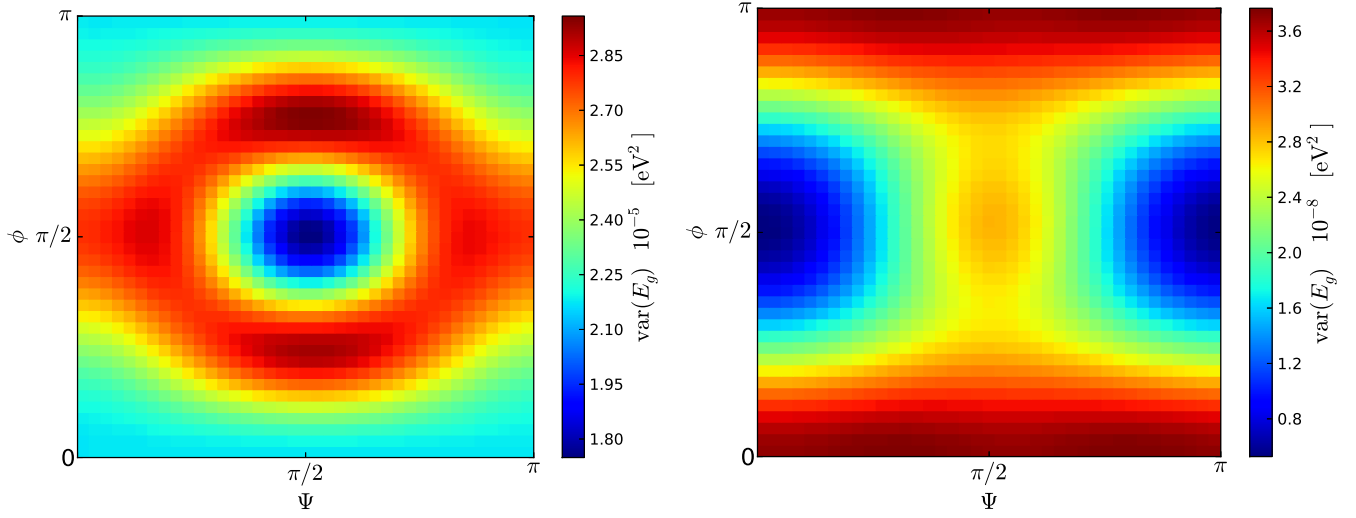


FIG. 6. Volume-weighted variance of the band-gap energy E_g with respect to Euler rotations $\mathbf{Z}_1(\theta=0)\mathbf{X}_2(\phi)\mathbf{Z}_3(\Psi)$ of the orientations of the monocrystalline shell elastic stiffness tensor axes away from the directions of the global coordinate system axes (which coincide with the orientations of the elastic stiffness tensor axes within the core region). For example, the $[111]$ orientation of the axes is achieved by setting $\theta = 0^\circ, \phi = 54.74^\circ$ and $\Psi = 45^\circ$, which corresponds to the top right corner of the bottom left quadrant. This CSNP model has total diameter of 25 nm and core/shell volume ratio of 0.276, and is relaxed under condition of vanishing external pressure. The left and right panels contain data for the Zn/*w*-ZnO and *w*-ZnO/*r*-TiO₂ systems, respectively.

* mangeri@phys.uconn.edu

- [1] Giuseppe Marci, Vincenzo Augugliaro, María J. López-Muñoz, Cristina Martín, Leonardo Palmisano, Vicente Rives, Mario Schiavello, Richard J. D. Tilley, and Anna Maria Venezia, "Preparation characterization and photocatalytic activity of polycrystalline ZnO/TiO₂ systems. 2. surface, bulk characterization, and 4-nitrophenol photodegradation in liquid/solid regime," *J. Phys. Chem. B* **105**, 1033–1040 (2001).
- [2] Qinghong Zhang, Wugang Fan, and Lian Gao, "Anatase TiO₂ nanoparticles immobilized on ZnO tetrapods as a highly efficient and easily recyclable photocatalyst," *Appl. Catal. B Environ.* **76**, 168–173 (2007).
- [3] Qing-lan Ma, Rui Xiong, Bao-gai Zhai, and Yuan Ming Huang, "Core-shelled Zn/ZnO microspheres synthesized by ultrasonic irradiation for photocatalytic applications," *Micro and Nano Letters* **8**, 491–495 (2013).
- [4] Marcel Bruchez Jr., Mario Moronne, Peter Gin, Shimon Weiss, and A. Paul Alivisatos, "Semiconductor Nanocrystals as Fluorescent Biological Labels," *Science* **281**, 2013–2015 (1998).
- [5] Jyoti K. Jaiswal, Hedi Mattoussi, J. Matthew Mauro, and Sanford M. Simon, "Long-term multiple color imaging of live cells using quantum dot bioconjugates," *Nat. Biotechnol.* **21**, 47–51 (2003).
- [6] X. Michalet, F.F. Pinaud, L. A. Bentolila, J. M. Tsay, S. Doose, J.J. Li, G. Sundaresan, A. M. Wu, S. S. Gambhir, and S. Weiss, "Quantum Dots for Live Cells, in Vivo Imaging, and Diagnostics," *Science* **307**, 538–544 (2005).
- [7] Yun Xing and Jianghong Rao, "Quantum dot bioconjugates for in vitro diagnostics & in vivo imaging," *Cancer Biomark.* **4**, 307–319 (2008).
- [8] Kwangjae Cho, Xu Wang, Shuming Nie, Zhuo Chen, and Dong M. Shin, "Therapeutic Nanoparticles for Drug Delivery in Cancer," *Clin. Cancer Res.* **14**, 1310–1316 (2008).
- [9] Juliana M. Chan, Liangfang Zhang, Kai P. Yuet, Grace Liao, June-Wha Rhee, Robert Langer, and Omid C. Farokhzad, "PLGA-lecithin-PEG core-shell nanoparticles for controlled drug delivery," *Biomaterials* **30**, 1627–1634 (2009).
- [10] Yueming Zhai, Junfeng Zhai, Ming Zhou, and Shaojun Dong, "Ordered magnetic core-manganese oxide shell nanostructures and their application in water treatment," *J. Mater. Chem.* **19**, 7030–7035 (2009).
- [11] Aihua Wu, Jin Jia, and Shengji Luan, "Amphiphilic PMMA/PEI core-shell nanoparticles as polymeric adsorbents to remove heavy metal pollutants," *Colloids Surf., A* **384**, 180–185 (2011).
- [12] Hongyun Niu, Dizhang, Zhaofu Meng, and Yaqi Cai, "Fast defluorination and removal of norfloxacin by alginate/Fe₃O₄ core/shell structured nanoparticles," *J. Hazard. Mater.* **227–228**, 195–203 (2012).
- [13] Xiaohui Guo, Yonghui Deng, Dong Gu, Renchao Che, and Dongyuan Zhao, "Synthesis and microwave absorption of uniform hematite nanoparticles and their core-shell mesoporous silica nanocomposites," *J. Mater. Chem.* **19**, 6706–6712 (2009).
- [14] Jiahua Zhu, Suying Wei, Neel Haldolaarachchige, David P. Young, and Zhanhu Guo, "Electromagnetic Field Shielding Polyurethane Nanocomposites Reinforced with Core-Shell Fe-Silica Nanoparticles," *J. Phys. Chem. C* **115**, 15304–15310 (2011).
- [15] Suying Wei, Qiang Wang, Jiahua Zhu, Luyi Sun, Hongfei Lin, and Zhanhu Guo, "Multifunctional composite core-shell nanoparticles," *Nanoscale* **3**, 4474–502 (2011).
- [16] R. G. Chaudhuri and Santanu Paria, "Core/shell nanoparticles: Classes, properties, synthesis mechanisms, characterization, and applications," *Chem. Rev.* **112**, 2373–2433 (2012).
- [17] Haibo Zeng, Weiping Cai, Jinlian Hu, Guotao Duan, Peisheng Liu, and Yue Li, "Violet photoluminescence from shell layer of ZnO core-shell nanoparticles induced by laser ablation," *Appl. Phys. Lett.* **88** (2006).
- [18] Newaz Mohammed Bahadur, Takeshi Furusawa, Masahide Sato, Fumio Kurayama, and Noboru Suzuki, "Rapid synthesis, characterization and optical properties of TiO₂ coated ZnO nanocomposite particles by a novel microwave irradiation method," *Mater. Res. Bull.* **45**, 1383–1388 (2010).
- [19] Prashant V. Kamat and Bhairavi Shanghavi, "Interparticle Electron Transfer in Metal/Semiconductor Composites. Picosecond Dynamics of CdS-Capped Gold Nanoclusters," *J. Phys. Chem. B* **101**, 39, 7675–7679 (1997).
- [20] Yu Lu, Yadong Yin, Zhi-Yuan Li, and Younan Xia, "Synthesis and Self-Assembly of Au@SiO₂ Core-Shell Colloids," *Nano Lett.* **2**, 785–788 (2002).
- [21] Min-Hung Liao, Chih-Hsiung Hsu, and Dong-Hwang Chen, "Preparation and properties of amorphous titania-coated zinc oxide nanoparticles," *J. Solid State Chem.* **179**, 2020–2026 (2006).
- [22] H. Y. Lin, Y. F. Chen, J. G. Wu, D. I. Wang, and C. C. Chen, "Carrier transfer induced photoluminescence change in metal-semiconductor core-shell nanostructures," *Appl. Phys. Lett.* **88**, 161911 (2006).
- [23] Xiangcun Li, Gaohong He, Gonkui Xiao, Hongjing Liu, and Mei Wang, "Synthesis and morphology control of ZnO nanostructures in microemulsions," *J. Colloid Interface Sci.* **333**, 465–473 (2009).
- [24] Sonalika Vaidya, Amitava Patra, and Ashok Kumar Ganguli, "CdS@TiO₂ and ZnS@TiO₂ core-shell nanocomposites: Synthesis and optical properties," *Colloids Surf., A* **363**, 130–134 (2010).
- [25] Matt Law, Lori E. Greene, Aleksandra Radenovic, Tevye Kuykendall, Jan Liphardt, and Peidong Yang, "ZnO - Al₂O₃ and ZnO - TiO₂ Core - Shell Nanowire Dye-Sensitized Solar Cells," *J. Phys. Chem.* **101**, 22652–22663 (2006).
- [26] Lori E. Greene, Matt Law, Benjamin D. Yuhas, and Peidong Yang, "ZnO-TiO₂ core-shell nanorod/p3ht solar cells," *J. Phys. Chem. C* **111**, 18451–18456 (2007).
- [27] Haibo Zeng, Weiping Cai, Bingqiang Cao, Jinlian Hu, Yue Li, and Peisheng Liu, "Surface optical phonon Raman scattering in ZnO core-shell structured nanoparticles," *Appl. Phys. Lett.* **88** (2006).
- [28] H. Zeng, Z. Li, W. Cai, B. Cao, P. Liu, and S. Yang, "Microstructure control of Zn/ZnO core/shell nanoparticles and their temperature-dependent blue emissions," *J. Phys. Chem. B* **111**, 14311–14317 (2007).
- [29] J. Q. Hu, Q. Li, X. M. Meng, C. S. Lee, and S. T. Lee, "Thermal reduction route to the fabrication of coaxial Zn/ZnO nanocables and ZnO nanotubes," *Chem. Mater.*

- 15**, 305–308 (2003).
- [30] Jih Jen Wu, Sai Chang Liu, Chien Ting Wu, Kuei Hsien Chen, and Li Chyong Chen, “Heterostructures of ZnO-Zn coaxial nanocables and ZnO nanotubes,” *Appl. Phys. Lett.* **81**, 1312–1314 (2002).
- [31] Y. J. Xing, Z. H. Xi, Z. Q. Xue, X. D. Zhang, J. H. Song, R. M. Wang, J. Xu, Y. Song, S. L. Zhang, and D. P. Yu, “Optical properties of the ZnO nanotubes synthesized via vapor phase growth,” *Appl. Phys. Lett.* **83**, 1689–1691 (2003).
- [32] Xiang Yang Kong, Yong Ding, and Zhong Lin Wang, “Metal/semiconductor ZnO core/shell nanobelts and nanotubes,” *J. Phys. Chem. B* **108**, 570–574 (2004).
- [33] Pu Xian Gao, Chang Shi Lao, Yong Ding, and Zhong Lin Wang, “Metal/semiconductor core/shell nanodisks and nanotubes,” *Adv. Funct. Mater.* **16**, 53–62 (2006).
- [34] O. Lupan, L. Chow, G. Chai, and H. Heinrich, “Fabrication and characterization of Zn-ZnO core-shell microspheres from nanorods,” *Chem. Phys. Lett.* **465**, 249–253 (2008).
- [35] Dai-ming Tang, Gang Liu, Feng Li, Jun Tan, Chang Liu, Gao Qing Lu, and Hui-ming Cheng, “Synthesis and Photoelectrochemical Property of Urchin-like Zn / ZnO Core - Shell Structures,” *J. Phys. Chem. C* **113**, 11035–11040 (2009).
- [36] D. L. Liao, C. a. Badour, and B. Q. Liao, “Preparation of nanosized TiO₂/ZnO composite catalyst and its photocatalytic activity for degradation of methyl orange,” *J. Photochem. Photobiol. A Chem.* **194**, 11–19 (2008).
- [37] Chang Sung Lim, “Processing Research Synthesis and characterization of TiO₂-ZnO nanocomposite by a two-step chemical method,” *J. Ceram. Process. Res.* **11**, 631–635 (2010).
- [38] I. Lun Hsiao and Yuh Jeen Huang, “Titanium oxide shell coatings decrease the cytotoxicity of ZnO nanoparticles,” *Chem. Res. Toxicol.* **24**, 303–313 (2011).
- [39] Rui Xiong, Bao-gai Zhai, Yuan Ming Huang, and Qing-lan Ma, “Core-shelled Zn/ZnO microspheres synthesised by ultrasonic irradiation for photocatalytic applications,” *Micro Nano Lett.* **8**, 491–495 (2013).
- [40] Hyoun Woo Kim, Seung Hyun Shim, and Jong Woo Lee, “Variation of ZnO shell thickness and its effects on the characteristics of coaxial nanowires,” *Nanotechnology* **19**, 145601 (2008).
- [41] Avijit Ghosh and R.N.P. Choudhary, “Optical emission and absorption spectra of ZnZnO core-shell nanostructures,” *J. Exp. Nanosci.* **5**, 134–142 (2010).
- [42] David A Drabold, Uwe Stephan, Jianjun Dong, and Serge M Nakhmanson, “The structure of electronic states in amorphous silicon,” *J. Mol. Graphics Mod.* **17**, 285–291 (1999).
- [43] CUBIT is developed by Sandia National Laboratories and is available at <https://cubit.sandia.gov/>.
- [44] Chris H. Rycroft, “VORO++: A three-dimensional Voronoi cell library in C++,” *Chaos* **19**, 99–100 (2009).
- [45] VORO++ is a software package for performing Voronoi tessellations on user-defined geometries and is available at <http://math.lbl.gov/voro++/>.
- [46] W. Halperin, “Quantum size effects in metal particles,” *Rev. Mod. Phys.* **58**, 533–606 (1986).
- [47] Masakazu Anpo, Takahito Shima, Sukeya Kodama, and Yutaka Kubokawa, “Photocatalytic Hydrogenation of CH₃CCH with H₂O on Small-particle TiO₂: Size Quantization Effects and Reaction Intermediates,” *J. Phys. Chem.* **91**, 4305–4310 (1987).
- [48] A. D. Yoffe, “Advances in Physics Low-dimensional systems : Quantum size effects and electronic properties of semiconductor microcrystallites (zero- dimensional systems) and some quasi-two-dimensional systems,” *Adv. Phys.* **51**, 799–890 (2002).
- [49] Kari Laasonen, Emanuele Panizon, Davide Bochicchio, and Riccardo Ferrando, “Competition between icosahedral motifs in agcu, agni, and agco nanoalloys: A combined atomistic - dft study,” *J. Phys. Chem. C* **117**, 26405–26413 (2013).
- [50] Davide Bochicchio and Riccardo Ferrando, “Morphological instability of core-shell metallic nanoparticles,” *Phys. Rev. B* **87**, 165435 (2013).
- [51] Emanuele Panizon and Riccardo Ferrando, “Preferential faceting of coherent interfaces in binary nanocrystals,” *Phys. Rev. B* **90**, 201410 (2014).
- [52] Riccardo Ferrando, “Symmetry breaking and morphological instabilities in core-shell metallic nanoparticles,” *J. Phys.: Condens. Matter* **27**, 013003 (2015).
- [53] J. F. Nye, *Physical Properties of Crystals* (Oxford University Press Inc., 1985).
- [54] H. M. Ledbetter, “Elastic properties of Zinc: a Compilation and a Review,” *J. Phys. Chem. Ref. Data* **6**, 1181–1203 (1977).
- [55] T. B. Bateman, “Elastic moduli of single-crystal zinc oxide,” *J. Appl. Phys.* **33**, 3309–3312 (1962).
- [56] D. G. Isaak, J. D. Carnes, O. L. Anderson, H. Cynn, and E. Hake, “Elasticity of TiO₂ rutile to 1800K,” *Phys. Chem. Miner.* **26**, 31–43 (1998).
- [57] Morton E. Gurtin and A. Ian Murdoch, “A continuum theory of elastic material surfaces,” *Arch. Ration. Mech. Anal.* **57**, 291–323 (1975).
- [58] J. Yvonnet, A. Mitrushchenkov, G. Chambaud, Q.-C. He, and S.-T. Gu, “Characterization of surface and nonlinear elasticity in wurtzite ZnO nanowires,” *J. Appl. Phys.* **111**, 124305 (2012).
- [59] Lan Jia, Da-Jun Shu, and Mu Wang, “Tuning the Area Percentage of Reactive Surface of TiO₂ by Strain Engineering,” *Phys. Rev. Lett.* **109**, 156104 (2012).
- [60] Markus R. Wagner, Gordon Callsen, Juan S. Reparaz, Ronny Kirste, Axel Hoffmann, Anna V. Rodina, André Schleife, Friedhelm Bechstedt, and Matthew R. Phillips, “Effects of strain on the valence band structure and exciton-polariton energies in ZnO,” *Phys. Rev. B* **88**, 235210 (2013).
- [61] Wan-Jian Yin, Shiyu Chen, Ji-Hui Yang, Xin-Gao Gong, Yanfa Yan, and Su-Huai Wei, “Effective band gap narrowing of anatase TiO₂ by strain along a soft crystal direction,” *Appl. Phys. Lett.* **96**, 221901 (2010).
- [62] FERRET is an open-source module for the MOOSE software package and is available at <https://bitbucket.org/mesosience/ferret>.
- [63] Dr Gaston, J Peterson, and Cj Permann, “Continuous integration for concurrent computational framework and application development,” *J. Open Res. Softw.* **2**, 1–6 (2013).
- [64] Derek Gaston, Chris Newman, Glen Hansen, Damien Lebrun-Grandie, and Damien Lebrun-Grandié, “MOOSE: A parallel computational framework for coupled systems of nonlinear equations,” *Nucl. Eng. Des.* **239**, 1768–1778 (2009).
- [65] Benjamin S. Kirk, John W. Peterson, Roy H. Stogner, and Graham F. Carey, “libMesh : a C++ library for par-

- allel adaptive mesh refinement/coarsening simulations,” Eng. Comput. **22**, 237–254 (2006).
- [66] The open-source MOOSE project is developed by Idaho National Laboratory and is available at <http://mooseframework.org/>.
- [67] Chris G. Van de Walle, “Band lineups and deformation potentials in the model-solid theory,” Phys. Rev. B **39**, 1871–1883 (1989).
- [68] J.-M. Wagner and F. Bechstedt, “Properties of strained wurtzite gan and aln: *Ab initio* studies,” Phys. Rev. B **66**, 115202 (2002).